RhRu Bimetallic Oxide Cluster Catalysts for Cross-Dehydrogenative Coupling of Arenes and Carboxylic Acids

Shingo Hasegawa,[1] Koji Harano,[2] and Ken Motokura*[1]

[1]Department of Chemistry and Life Science, Yokohama National University, 79-5 Tokiwadai, Hodogaya-ku, Yokohama 240-8501, Japan.

[2]Center for Basic Research on Materials, National Institute for Materials Science, 1-1 Namiki, Tsukuba, Ibaraki 305-0044, Japan.

KEYWORDS: bimetallic oxide cluster, noble metals, C–H bond activation, cross-dehydrogenative coupling

---

ABSTRACT: Noble-metal-based bimetallic oxide clusters are promising novel catalysts. In this study, we developed carbon-supported RhRu bimetallic oxide clusters ($RhRuO_x/C$) with a mean diameter of 1.2 nm, which showed remarkable catalytic activity for the cross-dehydrogenative coupling (CDC) of arenes and carboxylic acids with O_2 as the sole oxidant. RhRu bimetallic oxide cluster formation was confirmed by aberration-corrected high-angle annular dark-field scanning transmission electron microscopy with energy-dispersive X-ray spectroscopy and synchrotron X-ray absorption spectroscopy. Kinetic isotope and substituent effects indicated that arene C–H bond cleavage was the rate-determining step and proceeded via electrophilic concerted metalation–deprotonation mechanism, with a carboxylate as an internal base. Density functional theory calculations supported the proposed mechanism and indicated that the active center for C–H bond activation was Rh(V) rather than Rh(III), while Ru enhanced the electrophilicity of the Rh(V) site by decreasing the negative charge of the surrounding oxygen atoms. Electron-rich arenes showed relatively high reactivity for $RhRuO_x/C$-catalyzed CDC reaction, and both aliphatic and aromatic carboxylic acids were applicable to the reaction. The $RhRuO_x/C$ catalyst is promising for the CDC reaction of arenes and carboxylic acids to produce aryl esters. This work will promote the development of noble-metal-based bimetallic oxide clusters for C–H bond activation reactions.

Introduction. Bimetallic nanoparticles (NPs) and clusters have attracted great interest owing to their enhanced or novel catalysis derived from unique geometric and electronic structures.[1,2] In particular, noble-metal-based bimetallic catalysts have been intensively developed, and their high catalytic performance has been demonstrated for various hydrogenation, oxidation, dehydrogenation, electrocatalytic, photocatalytic, and synthetic reactions.[3–19] However, the noble metals in the bimetallic catalysts in such reaction systems tend to have oxidation states of zero. Furthermore, noble-metal-based bimetallic oxide NP and cluster catalysts have not been extensively studied. Bimetallic oxide clusters based on group III–VII metals, known as heteropolyoxometalates, are excellent catalysts for various reactions, such as acid-catalyzed and oxidation reactions.[20–24] Therefore, exploring the catalysis of noble-metal-based bimetallic oxide clusters is an interesting research target.

Cross-dehydrogenative coupling (CDC) reactions between aromatic C–H and X–H (X = C, N, O) bonds have recently attracted considerable interest owing to their step/atom economy.[25–31] CDC reactions between arenes and carboxylic acids can produce aryl esters directly from nonactivated substrates.[28] Homogeneous catalysts such as Co,[32] Ru,[33–35] Rh,[36–40] Pd,[41–49] and Au[50,51] complexes have been developed for the coupling of arenes and carboxylic acids (**Figure 1a**). Oxidants are generally required for these reactions to occur. Representative oxidants include phenyliodine(III) diacetate (PIDA) and persulfate and silver salts. However, molecular oxygen is a preferable oxidant in terms of atom economy, availability, and nontoxicity.[29] Shindo *et al*. reported heterogeneous CDC reactions with O_2 as the sole oxidant, where polycyclic aromatics and CX_3COOH (X = F, Cl) were applicable substrates (**Figure 1b**).[52] Thus, there is still need for exploration of heterogeneous catalysts utilizing O_2 as the sole oxidant with wide applicability to arenes and aliphatic/aromatic carboxylic acids.

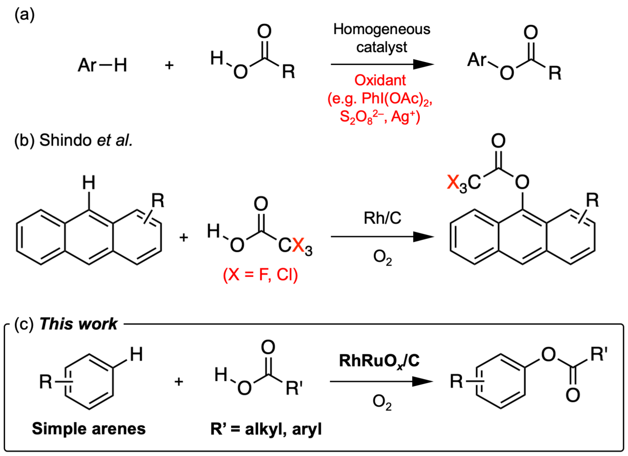

Figure 1. CDC reactions of arenes and carboxylic acids catalyzed by (a) homogeneous catalysts, (b) carbon-supported Rh (Rh/C), and (c) carbon-supported RhRu bimetallic oxide cluster (RhRuO$_x$/C) (this work).

In this study, we found that a carbon-supported RhRu bimetallic oxide cluster (RhRuO$_x$/C) catalyst showed much higher catalytic activity for the CDC reaction of benzene and acetic acid (**Figure 1c**) than other noble-metal-based monometallic and bimetallic catalysts. Detailed structural analyses using aberration-corrected high-angle annular dark-field scanning transmission electron microscopy (AC-HAADF-STEM) and synchrotron X-ray absorption spectroscopy (XAS) revealed the formation of bimetallic oxide clusters on the carbon support. The clusters had a narrow size distribution and an average diameter of 1.2 nm. Mechanistic studies using substituted and deuterated benzenes indicated that the CDC reaction proceeded via electrophilic and concerted C–H bond activation by the Rh–acetate site of RhRuO$_x$ and that Ru enhanced the electrophilicity of the Rh active center to promote the rate-determining C–H bond activation step. RhRuO$_x$/C was applicable to reactions with various arenes and carboxylic acids using O_2 as the sole oxidant. We believe that this study opens a novel research paradigm for noble metal-based bimetallic oxide cluster catalysts.

Results and Discussion.

Catalyst Optimization. We initially screened several carbon-supported noble-metal-based monometallic catalysts, namely, Rh/C, Pt/C, Ir/C, Ru/C, Pd/C, Au/C, and Ag/C. The catalysts were prepared by depositing preformed metal particles on carbon supports. The metal particles were synthesized using a conventional polyol method;[53] metal salts were treated at 180 °C in the presence of NaOH using ethylene glycol as the solvent. The activities of the prepared catalysts for the CDC reaction of arenes and carboxylic acids were evaluated using benzene (**1a**) and acetic acid (**2a**) as model substrates (**Figure 2a**). The reactions were carried out at 150 °C in 0.5 MPa O_2 as the sole oxidant. Rh/C exhibited a much higher yield of phenyl acetate (**3aa**) than the other monometallic catalysts (**Figure 2b**). Although the formation of biphenyl (**4a**) was confirmed, Rh/C showed high selectivity (98%) toward the CDC product, **3aa**. The Ir, Ru, and Au catalysts also selectively catalyzed the CDC reaction, whereas comparable amounts of **4a** and **3aa** were formed when using the Pt and Pd catalysts. Notably, the **3aa** yield of Rh/C (270 μmol) was significantly higher than that of a commercially available carbon-supported Rh catalyst (98 μmol).

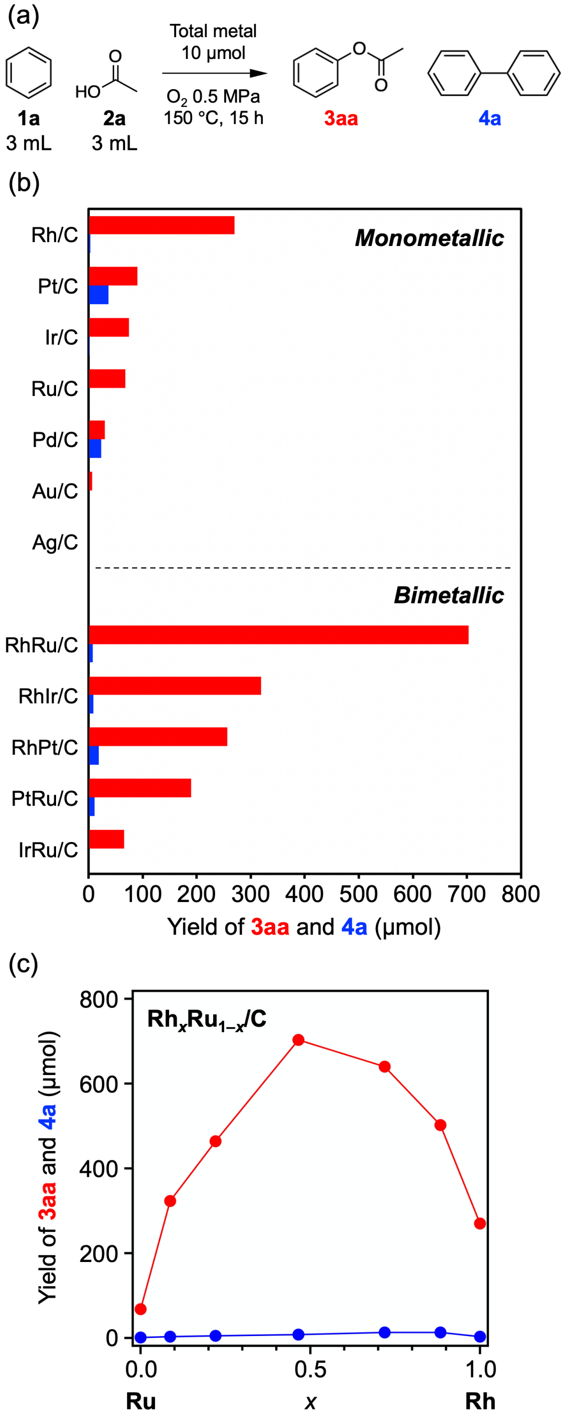

Figure 2. (a) CDC reaction of benzene (**1a**) and acetic acid (**2a**). (b) Yield of **3aa** (red) and **4a** (blue) using various monometallic and bimetallic catalysts (total metal amount: 10 μmol). (c) Yield of **3aa** (red) and **4a** (blue) using RhRu bimetallic catalyst (Rh_xRu_{1-x}/C) as a function of x.

We also screened several noble-metal-based bimetallic catalysts, namely, RhRu/C, RhIr/C, RhPt/C, PtRu/C, and IrRu/C, for the CDC reaction. These catalysts were prepared by synthesizing metal colloids from an equimolar mixture of precursors and depositing them on carbon supports. The **3aa** and **4a** yields using these catalysts (total metal amount: 10 μmol) are shown in **Figure 2b**. Remarkable synergy between Rh and Ru was observed: RhRu/C had a **3aa** yield of 703 µmol, which was more than 2.5 times that of Rh/C (270 µmol), while retaining high selectivity for **3aa**. By contrast, RhIr/C and RhPt/C exhibited comparable catalytic activities to that of Rh/C. The effect of the Rh/Ru molar ratio was further studied. The **3aa** and **4a** yields of various Rh_xRu_{1-x}/C catalysts are plotted against the Rh content (x) in **Figure 2c**. Synergy between Rh and Ru was observed for all Rh_xRu_{1-x}/C catalysts, although the highest catalytic activity was achieved at a molar ratio of ~1:1.

When the catalyst precursors ($RhCl_3$ and $RuCl_3$) were used separately and together as homogeneous catalysts for the CDC reaction, the catalytic activities were much lower than that of RhRu/C, with **3aa** yields of less than 2 µmol (**Table S2**). In addition, no synergistic effect was observed between $RhCl_3$ and $RuCl_3$. Moreover, separating RhRu/C from the reaction system by filtration completely stopped the reaction (**Figure S1**). The catalytic activity of recovered RhRu/C did not show dramatic decrease compared to that of the fresh catalyst (**Figure S2**). These results suggest that the active species for the CDC reaction are not leached metal species but rather the metal particles on the carbon support.

Structural Analysis of RhRu Catalyst. The particle size and elemental distribution of RhRu/C were analyzed using AC-HAADF-STEM with energy-dispersive X-ray spectroscopy (EDS). A representative HAADF image of RhRu/C is presented in **Figure 3a**. The observed metal particles had a narrow size distribution and diameter of 1.2 ± 0.2 nm (mean ± standard deviation) (**Figure 3b**). Furthermore, atomic-resolution images of ~1 nm sized particles were successfully obtained (**Figure 3c**).

Size Distribution

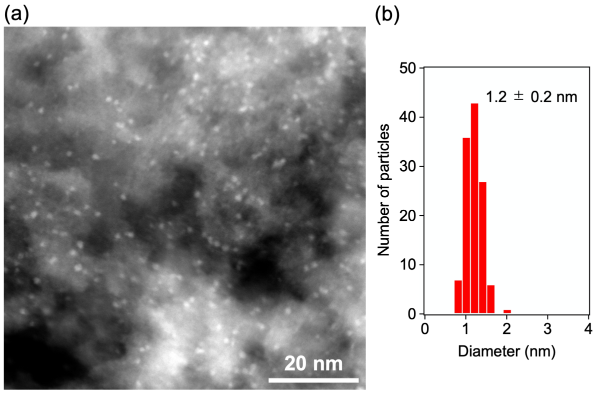

Atomic Resolution Image

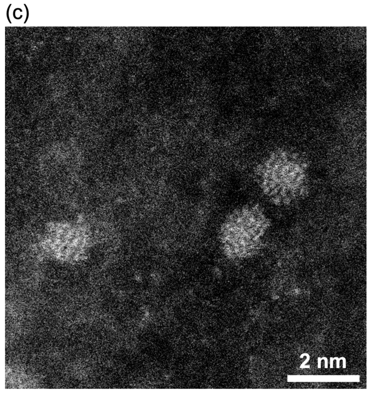

Figure 3. Size distribution of RhRu/C: (a) representative HAADF image and (b) histogram of particle diameters. (c) Atomic resolution HAADF image.

The EDS mapping results of the region in **Figure 4a** are shown in **Figures 4b–f**. The distributions of Rh and Ru showed good agreement (**Figure 4f**), indicating the coexistence of Rh and Ru in individual particles. We successfully analyzed a single particle using EDS (**Figures S3** and **S4**) and found that Rh and Ru were homogeneously distributed within the particle. The Rh/Ru atomic ratio in the particle was 45:55, as calculated by quantitative analysis of the EDS spectrum, which is in reasonable agreement with the inductively coupled plasma–atomic emission spectrometry result (Rh/Ru = 47:53; **Table S1**). EDS analysis of a larger area yielded a similar result; for example, the Rh/Ru atomic ratio in the area corresponding to **Figure 4a** was 46:54 (**Figure S5**).

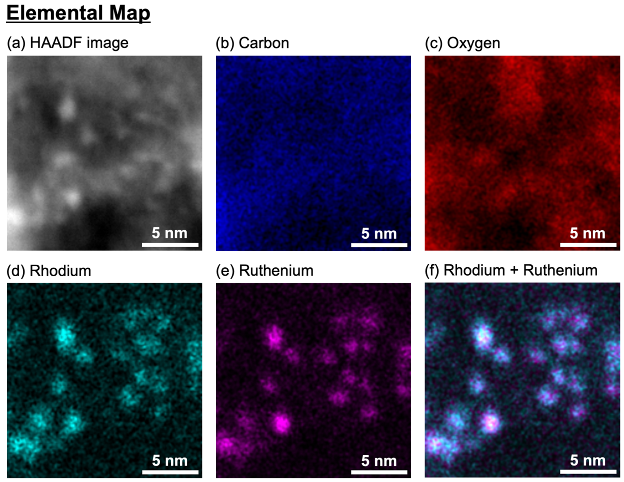

Figure 4. Elemental mapping results of RhRu/C: (a) HAADF image of the area analyzed by EDS and elemental maps of (b) carbon, (c) oxygen, (d) rhodium, and (e) ruthenium. (f) Overlay of rhodium and ruthenium distributions.

The electronic structures and coordination environments of Rh and Ru in RhRu/C were studied by XAS. The Rh and Ru K-edge X-ray absorption near-edge structures (XANES) are shown in **Figures 5a** and **5b**, respectively. The spectra resemble those of the metal oxides (Rh_2O_3 and RuO_2, respectively), indicating that Rh and Ru exist in an oxidized state. Consistent results were obtained by the analysis of Rh and Ru K-edge extended X-ray absorption fine structures (EXAFS; **Figure S6**); the Fourier-transform EXAFS spectra contained peaks corresponding to Rh–O and Ru–O bonds, respectively, whereas no clear peaks of direct metal–metal bond were observed (**Figures 5c** and **5d**). Curve-fitting analysis with metal–oxygen bonds showed reasonable agreement between the experimental and fitting data (**Table 1**). The coordination numbers (CNs) of the Rh–O and Ru–O bonds were calculated to be 3.2 ± 0.3 and 3.2 ± 0.3, respectively. These low CNs suggested that the metal atoms are coordinatively unsaturated and can be active sites for CDC reactions. According to XAS of other monometallic and bimetallic catalysts, Rh, Pt, Ir, and Ru species are also fully oxidized, except for partially oxidized Ir in monometallic Ir/C (**Figures S7** and **S8**).

Collectively, the structural analyses using AC-HAADF-STEM and XAS indicate the formation of RhRu bimetallic oxide clusters ($RhRuO_x$) on the carbon support. Because the Rh and Ru K-edge XAFS of the RhRu colloids before deposition corresponded to metallic states (**Figure S9**), the oxidation of Rh and Ru occurred during the deposition process conducted in air. Rh/C and Ru/C also formed oxide clusters (RhO_y and RuO_z, respectively) with sizes similar to those of $RhRuO_x$/C (**Figures S8** and **S10**, **Table S3**). Thus, the significantly higher catalytic activity of $RhRuO_x$/C cannot be ascribed to differences in particle size.

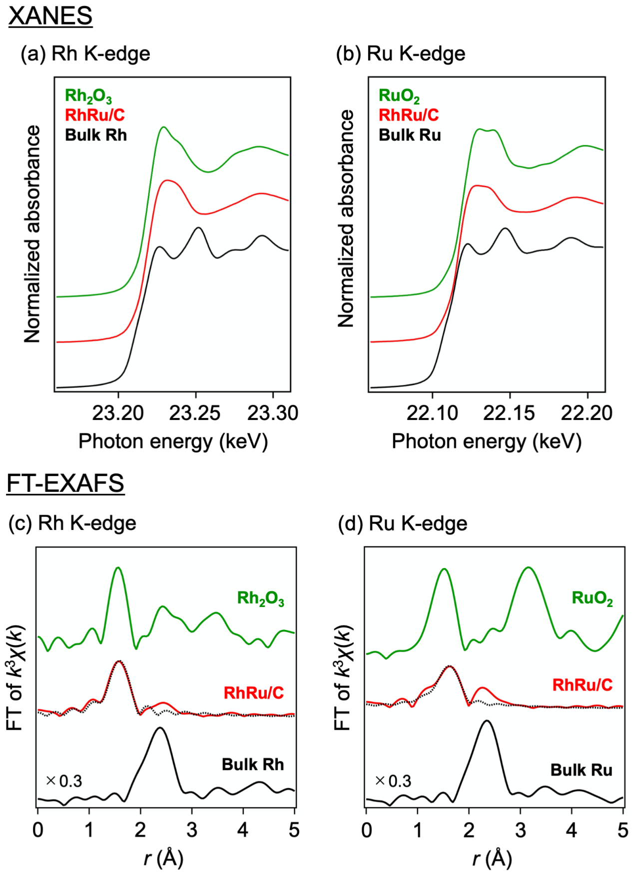

Figure 5. XAS results of RhRu/C. (a) Rh and (b) Ru K-edge XANES spectra. Fourier transform of (c) Rh and (d) Ru K-edge EXAFS spectra. Solid and dashed curves correspond to experimental and fitting data, respectively.

Table 1. Structural parameters obtained by curve-fitting analysis of Rh and Ru K-edge EXAFS

Edge	Sample	Bond	CN [a]	r (Å) [b]	σ^2 (Å^2) [c]	R (%) [d]
Rh K	RhRu/C	Rh–O	3.2 ± 0.3	2.04 ± 0.01	0.0034 ± 0.0017	5.6
Ru K		Ru–O	3.2 ± 0.3	2.07 ± 0.01	0.0077 ± 0.0023	8.1

[a] Coordination number. [b] Bond length. [c] Debye-Waller factor. [d] $R = [\sum\{k^3\chi^{data}(k) - k^3\chi^{fit}(k)\}^2]^{1/2}/[\sum\{k^3\chi^{data}(k)\}^2]^{1/2}$

Characterization of the $RhRuO_x$/C catalyst after the CDC reaction revealed that the $RhRuO_x$ clusters did not undergo large structural changes. Size evaluation using transmission electron microscopy revealed similar average diameters before and after the reaction (**Figure S11**). The white line intensity in the Rh and Ru K-edge XANES and the CNs of the metal–oxygen bonds both increased slightly following the reaction (**Figure S12**, **Table S4**), confirming that the RhRu bimetallic oxide clusters provided the active sites for the catalytic reaction.

Mechanistic Studies. To gain insight into the reaction mechanism, the effects of isotopes and substituents on the CDC reaction using the $RhRuO_x/C$ catalyst were studied and compared to those using a RhO_y/C catalyst. The kinetic isotope effect (KIE) was evaluated by comparing the reaction rates of benzene and benzene-d_6 (**Figure 6a**). Primary KIE values of 2.4 and 2.8 were obtained for $RhRuO_x/C$ and RhO_y/C, respectively. These results indicate that C–H bond cleavage was the rate-determining step for both catalytic systems. The turnover frequencies (TOFs) of $RhRuO_x/C$ and RhO_y/C for substituted benzenes (anisole, toluene, and bromobenzene; R = OMe, Me, and Br, respectively) are shown in **Figure 6b**. In both cases, the TOF increased as the electron-donating ability of the substituent increased. According to previous studies, this trend suggests two possible reaction mechanisms: (1) electrophilic aromatic substitution (S_EAr) mechanism and (2) base-assisted internal electrophilic substitution/electrophilic concerted metalation deprotonation (BIES[54-59]/*e*CMD[60-64]) mechanism. The reactions by S_EAr mechanism generally show small KIE values;[65,66] for instance, KIE of 1.0 was reported for Rh-catalyzed intramolecular C-H bond amination.[66] Considering the primary KIE values, it was concluded that C–H bond activation on $RhRuO_x/C$ and RhO_y/C (KIE: 2.4 and 2.8, respectively) proceeded via *e*CMD mechanism, with a carboxylate as an internal base (**Figure 7**). The addition of KOAc did not increase the initial reaction rate of the CDC reaction of benzene and acetic acid (**Figure S13**), supporting the intramolecularly carboxylate-assisted mechanism.[67-69] The reason for the decrease of reaction rate is probably the suppression of arene coordination to cluster surface by excess acetate ligands. Furthermore, because the KIE value of $RhRuO_x/C$ (2.4) was slightly lower than that of RhO_y/C (2.8), Ru likely promoted the rate-determining C–H bond activation step. As discussed later by DFT calculations, Ru possibly enhances the electrophilicity of the Rh center in the bimetallic $RhRuO_x/C$ system.

(a) Kinetic isotope effect

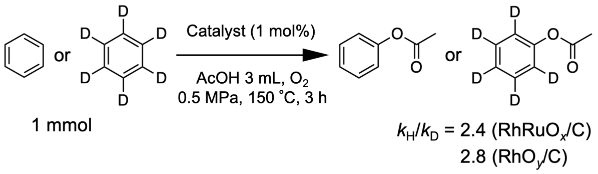

(b) Substituent effect

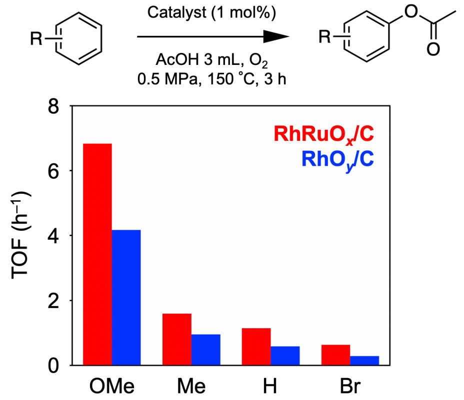

Figure 6. Mechanistic studies of $RhRuO_x/C$ and RhO_y/C catalysts. (a) CDC reaction of benzene or benzene-d_6 with acetic acid for the evaluation of KIE. (b) TOF for substituted benzenes (R = OMe, Me, H, and Br). For $RhRuO_x/C$, TOF was calculated based on the total metal amount.

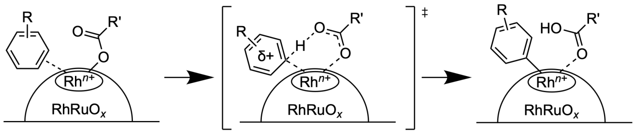

Figure 7. Proposed *e*CMD mechanism for rate-determining C–H bond activation step on $RhRuO_x/C$.

The reaction mechanism of the rate-determining C–H bond activation step was studied by density functional theory (DFT). Calculations were performed using Gaussian 16[70] with the B3LYP-D3 functional.[71–73] Solvent effects were included by the polarizable continuum model with parameters for acetic acid. First, we examined the reaction mechanism of the monometallic RhO_y/C system. A single Rh_4O_6 cluster (without the carbon support) was employed as the model catalyst because of its highly symmetrical structure with pseudo-T_d symmetry (**Figure S14a**). Similar structures have been experimentally observed in gas phase studies on rhodium oxide cluster cations isolated in vacuum.[74,75] Considering that acetoxylation and some other C–H activation reactions of arenes catalyzed by Rh complexes proceed by Rh(III)/Rh(V) redox cycling,[37–39,76–78] and that our reaction system was operated under a high O_2 pressure and high temperature, we examined both Rh(III)–acetate and Rh(V)–acetate species (in $Rh_4O_5(OAc)_2$ and $Rh_4O_6(OAc)_2$ cluster models, respectively; **Figures S14b** and **S14c**) as candidates for the active center of the C–H bond activation reaction (**Figure 8**). Calculated Gibbs free energies of the model clusters suggested that the generation of Rh(V) species on the Rh oxide clusters by O_2 is thermodynamically possible. The Gibbs free energy of the following reaction (*ΔG*) was calculated to be negative (-79 kJ/mol, **Figure S15**):

$$Rh_4O_6 + 2\ AcOH + 1/2\ O_2 \rightarrow Rh_4O_6(OAc)_2 + H_2O$$

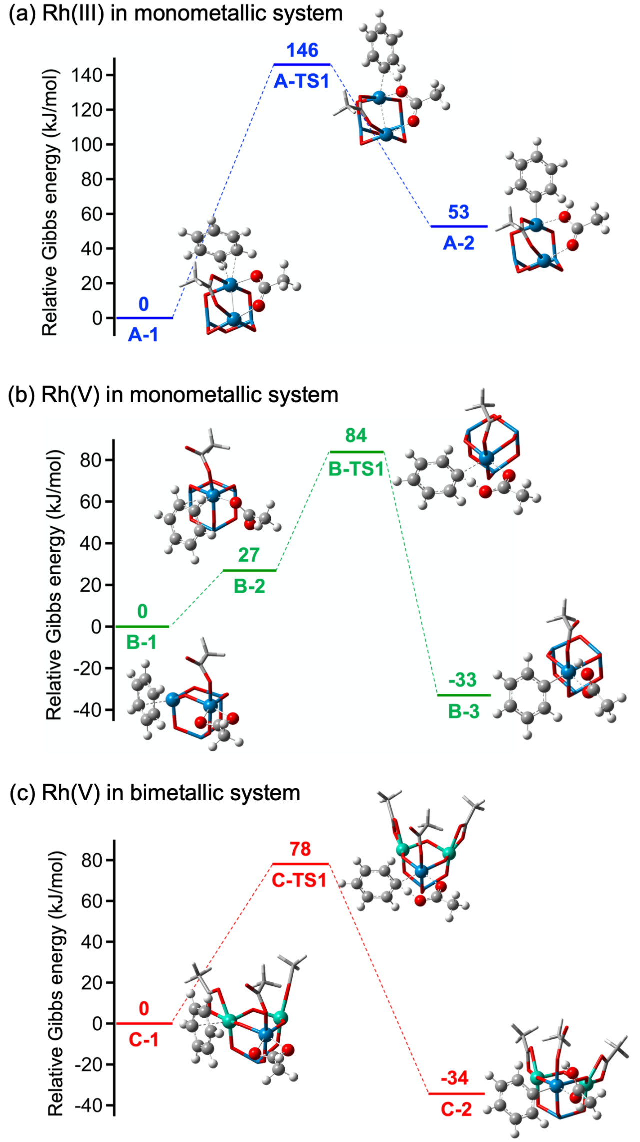

Figure 8. Free energy profiles of C–H bond activation by different Rh sites with acetate ligands: (a) Rh(III) site of $Rh_4O_5(OAc)_2$, (b) Rh(V) site of $Rh_4O_6(OAc)_2$, and (c) Rh(V) site of $Rh_2Ru_2O_5(OAc)_4$. C, H, O, Rh, and Ru are colored gray, white, red, blue, and green, respectively.

The Gibbs free energy of C–H bond activation of benzene was calculated for the model clusters with Rh(III)–OAc and Rh(V)–OAc active sites. The calculated free energy profiles are illustrated in **Figures 8a** and **8b**, respectively, along with the optimized structures of each state. The Rh(V)–OAc site had a significantly lower activation barrier (84 kJ/mol) than the Rh(III)–OAc site (146 kJ/mol), suggesting that the Rh(V) species is a more plausible active site. At transition states of **A-TS1** and **B-TS1**, Rh–C and O–H bond formation and C–H bond dissociation simultaneously proceeded. The Gibbs free energies of C–H activation for substituted benzenes (anisole and bromobenzene) were calculated for the Rh(V) model (**Figure S16**, **Table 2**). The calculated activation barrier decreased as the electron-donating ability of the substituent increased. The electrophilic nature of the active center was also confirmed by bond order analysis of the initial, transition, and final states of the C–H activation reaction.[57,60–62,64] The More O'Ferrall–Jencks plots of the Wiberg bond orders of the Rh–C and C–H bonds (**Figure 9a**) calculated for C–H activation of benzene, anisole, and bromobenzene (**Figures 9b**, **S18a**, and **S18b**, respectively) revealed that the transition states were located to the right of the fully concerted trajectory lines connecting the initial and final states. This indicates that Rh–C bond formation partially preceded C–H bond scission. Overall, the theoretical results indicate that arene C–H bond activation proceeded at the Rh(V) center of RhO$_y$/C via *e*CMD mechanism, which is consistent with the experimental observations.

Table 2. Gibbs free energy of C–H activation at Rh(V) site of monometallic and bimetallic oxide clusters

Cluster	$\Delta G^{\ddagger}$ (kJ/mol)		
	Ph–OMe	Ph–H	Ph–Br
$Rh_4O_6(OAc)_2$	82	84	90
$Rh_2Ru_2O_6(OAc)_4$	76	78	83

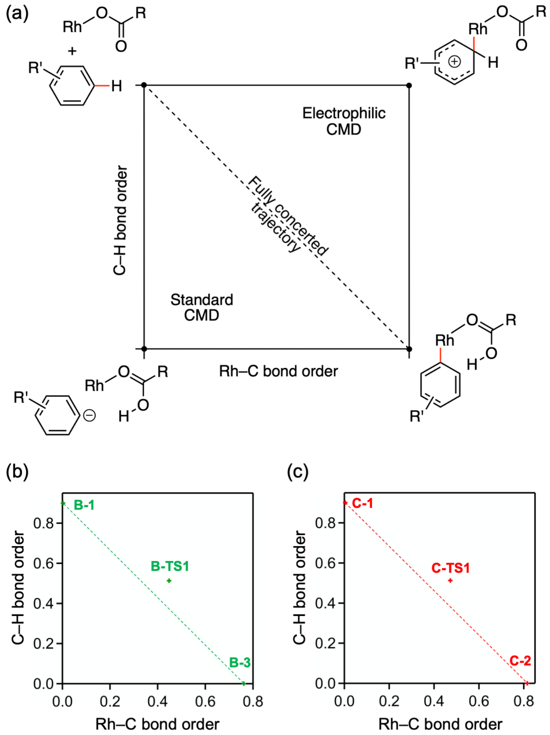

Figure 9. (a) Schematic illustration of More O'Ferrall-Jencks plot for metal-catalyzed C–H activation. (b, c) More O'Ferrall-Jencks plots of Wiberg bond orders calculated for systems **B** and **C** corresponding to **Figures 8b** and **8c**, respectively.

A model of the bimetallic RhRuO$_x$/C catalyst was constructed by modifying the $Rh_4O_6(OAc)_2$ model. Specifically, the two Rh(III) sites were replaced by Ru(IV) atoms with acetate ligands to obtain $Rh_2Ru_2O_6(OAc)_4$ (**Figure S14d**). Free energy diagrams of the C–H bond activation of benzene, anisole, and bromobenzene in bimetallic system are shown in **Figures 8c, S17a,** and **S17b**, respectively. For each arene, bimetallic system showed lower activation Gibbs energy than that in the monometallic system (**Table 2**), which is consistent with the experimental result. The calculated activation barrier in bimetallic system decreased as the electron-donating ability of the substituent increased. In the More O'Ferrall-Jencks plots of arene C–H bond activation in bimetallic system (**Figures 9c, S18c, S18d**), transition states are located within the *e*CMD region. These theoretical results supported *e*CMD mechanism for RhRuO$_x$/C-catalyzed C–H activation. Although there was no direct bonding between Rh(V) and Ru(IV) in the model cluster, the introduction of Ru(IV) to the second-nearest neighboring sites of the active center decreased the activation barrier. The charge distribution around the Rh(V) site was analyzed to obtain a deeper understanding of the effect of replacing Rh(III) with Ru(IV). The atomic charges before and after substitution are illustrated in **Figure S19**. The most significant change was observed for the O atoms bridging Rh(V) and Ru(IV); specifically, the absolute values of the negative charges on these atoms decreased upon substitution. Thus, Ru(IV) indirectly enhanced the electrophilicity of the Rh(V) active center via the reduction of the net negative charge on the surrounding O atoms. Based on the experimental and theoretical considerations, a catalytic cycle for the CDC reaction of arenes and carboxylic acids catalyzed by RhRuO$_x$/C was proposed (**Figure 10**).

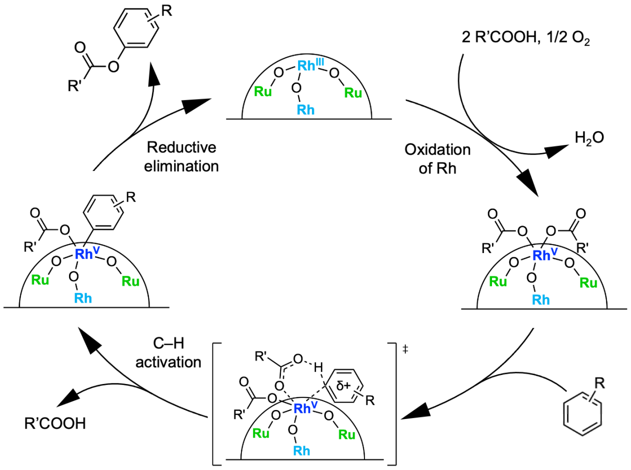

Figure 10. Proposed catalytic cycle for the CDC reaction of arenes and carboxylic acids catalyzed by RhRuO$_x$/C.

Substrate scope. The applicability of the RhRuO$_x$/C catalyst to CDC reactions using various arenes (**1a**–**i**) and carboxylic acids (**2a**–**e**) was examined (**Figure 11**). The acetoxylation reactions of arenes (**1a**–**i**, 1 mmol) and acetic acid (**2a**, 2.7 mL) using RhRuO$_x$/C (total metal amount: 10 μmol) are summarized in **Figure 11a**. The reactions were conducted in the presence of acetic anhydride (0.3 mL) and O$_2$ (0.8 MPa) at 150 °C for 15 h. As observed in the mechanistic studies above, electron-rich arenes showed higher reactivity than electron-poor ones. The acetoxylation of 1,2-dimethoxybenzene (**1b**) afforded both mono- and di-acetoxylated products (total yield: 78%) at a ratio of 69:31. The reaction of **1b** could be conducted under milder reaction conditions (120 °C, O$_2$ 0.3 MPa) and the products were obtained with a yield of 77% (mono:di=71:29) after 48 h using 5 mol% of the catalyst. The reactivity of 1,4-dimethoxybenzene (**1c**) was significantly lower than that of **1b**, which was ascribed to steric effects. C(aryl)–H bond activation by supported Au and Ru catalysts preferentially occurs at less sterically hindered positions because the catalyst surface acts as a bulky ligand.[79,80] Consistently, the acetoxylation of mono-substituted benzenes (**1e, 1f**, **1h**, and **1i**) showed low selectivity to *ortho*-position. The reactions of arenes containing classical simple directing groups such as 2-phenylpyridine and *N*-methylbenzamide afforded almost no product. This observation was ascribed to the sterically crowded transition state structure of C–H activation by the Rh(V) site. In the case of benzene, the Rh(V) center in the transition state (**B-TS1**, **Figure 8b**) is hexacoordinated, where additional coordination by an arene with directing group is not suitable.

The scope of carboxylic acids **2b**–**e** was examined using electron-rich arenes **1b** and **1e** (**Figure 11b**). Both aliphatic and aromatic carboxylic acids were applicable to this reaction system.

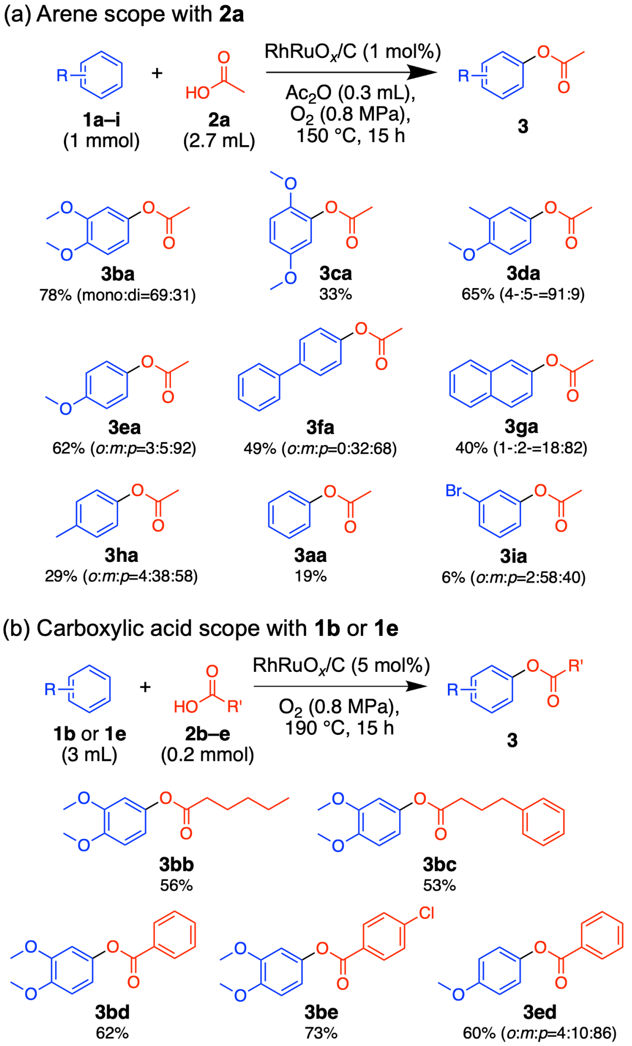

Figure 11. (a) Scope of arenes for acetoxylation. (b) Scope of carboxylic acids for CDC reaction with electron rich arenes.

Conclusions. In this study, we prepared a carbon-supported RhRu bimetallic oxide cluster catalyst, RhRuO$_x$/C, using a simple and reproducible method. RhRuO$_x$/C showed much higher catalytic activity for the CDC reaction of benzene and acetic acid than other noble-metal-based mono- and bimetallic catalysts owing to the synergistic effect between Rh and Ru. The formation of bimetallic oxide clusters with a homogeneous size distribution, mean diameter of 1.2 ± 0.2 nm, and coordinatively unsaturated metal sites was confirmed by AC-HAADF-STEM, EDS, and synchrotron XAS. The kinetic isotope and substituent effects on the CDC reaction of benzene and acetic acid indicated that C–H bond cleavage was the rate-determining step and proceeded via *e*CMD mechanism at the Rh–carboxylate site of $RhRuO_x$. DFT calculations of arene C–H bond activation by model oxide clusters suggested that Rh(V)–carboxylate species were the active centers for C–H activation. The dependence of the calculated Gibbs free energies of C–H activation on the benzene substituent and the results of bond order analysis provided further evidence for the *e*CMD mechanism. The promotional effect of Ru on C–H activation was observed for all calculated systems, and charge analysis suggested that Ru indirectly enhanced the electrophilicity of the Rh active center by decreasing the negative charges of the O atoms coordinating to the Rh center. Finally, $RhRuO_x/C$ was applicable for the CDC reactions of various arenes and carboxylic acids using O_2 as the sole oxidant. The findings of this study will contribute to the further development of noble-metal-based bimetallic oxide clusters for C–H bond activation reactions.

ASSOCIATED CONTENT

Supporting Information

The Supporting Information is available free of charge on the ACS Publications website.

Experimental details, results of elemental analysis, additional data of catalytic reactions, EDS images and spectra, XAS data, TEM images, DFT-optimized structures, calculated free energy profiles, results of bond order and population analyses, characterization data of new compounds, and Cartesian coordinates of optimized structures. (PDF)

AUTHOR INFORMATION

Corresponding Author

Ken Motokura – Department of Chemistry and Life Science, Yokohama National University, Yokohama 240-8501, Japan
E-mail: motokura-ken-xw@ynu.ac.jp

Authors

Shingo Hasegawa – Department of Chemistry and Life Science, Yokohama National University, Yokohama 240-8501, Japan
Koji Harano – Center for Basic Research on Materials, National Institute for Materials Science, Ibaraki 305-0044, Japan

Notes

The authors declare no competing financial interest.

ACKNOWLEDGMENT

The authors thank Dr. Jun Kikkawa (NIMS) for assistance with the STEM experiments. This research was financially supported by JSPS KAKENHI (Grant Nos. JP22K20554, JP23K13602, and JP23H04874) and the Tokyo Ohka Foundation for the Promotion of Science and Technology. The calculations were partly performed at the Research Center for Computational Science, Okazaki, Japan (Projects 22-IMS-C237 and 23-IMS-C283). The synchrotron XAS measurements were conducted with the approval of the Photon Factory Advisory Committee (Proposal No. 2022G033).

REFERENCES

1. Liu, L.; Corma, A. Bimetallic Sites for Catalysis: From Binuclear Metal Sites to Bimetallic Nanoclusters and Nanoparticles *Chem. Rev.* **2023**, *123*, 4855–4933.
2. Nakaya, Y.; Furukawa, S. Catalysis of Alloys: Classification, Principles, and Design for a Variety of Materials and Reactions. *Chem. Rev*. **2023**, *123*, 5859–5947.
3. Ding, K.; Cullen, D. A.; Zhang, L.; Cao, Z.; Roy, A. D.; Ivanov, I. N.; Cao, D. A General Synthesis Approach for Supported Bimetallic Nanoparticles via Surface Inorganometallic Chemistry. *Science* **2018**, *362*, 560-564.
4. Nakagawa, Y.; Takada, K.; Tamura, M.; Tomishige, K. Total Hydrogenation of Furfural and 5-Hydroxymethylfurfural over Supported Pd-Ir Alloy Catalyst. *ACS Catal.* **2014**, *4*, 2718-2726.
5. Tang, M.; Mao, S.; Li, M.; Wei, Z.; Xu, F.; Li, H.; Wang, Y. RuPd Alloy Nanoparticles Supported on N-Doped Carbon as an Efficient and Stable Catalyst for Benzoic Acid Hydrogenation. *ACS Catal.* **2015**, *5*, 3100-3107.
6. Huang, B.; Kobayashi, H.; Yamamoto, T.; Matsumura, S.; Nishida, Y.; Sato, K.; Nagaoka, K.; Kawaguchi, S.; Kubota, Y.; Kitagawa, H. Solid-Solution Alloying of Immiscible Ru and Cu with Enhanced CO Oxidation Activity. *J. Am. Chem. Soc*. **2017**, *139*, 4643-4646.
7. Chen, G.; Zhao, Y.; Fu, G.; Duchesne, P. N.; Gu, L.; Zheng, Y.; Weng, X.; Chen, M.; Zhang, P.; Pao, C.-W.; Lee, J.-F.; Zheng, N. Interfacial Effects in Iron-Nickel Hydroxide–Platinum Nanoparticles Enhance Catalytic Oxidation. *Science* **2014**, *344*, 495-499.
8. Wu, C. H.; Liu, C.; Su, D.; Xin, H. L.; Fang, H.-T.; Eren, B.; Zhang, S.; Murray, C. B.; Salmeron, M. B. Bimetallic synergy in cobalt–palladium nanocatalysts for CO oxidation. *Nat. Catal.* **2019**, *2*, 78-85.
9. Huang, X.; Akdim, O.; Douthwaite, M.; Wang, K.; Zhao, L.; Lewis, R. J.; Pattisson, S.; Daniel, I. T.; Miedziak, P. J.; Shaw, G.; Morgan, D. J.; Althahban, S. M.; Davies, T. E.; He, Q.; Wang, F.; Fu, J.; Bethell, D.; McIntosh, S.; Kiely, C. J.; Hutchings, G. J. Au–Pd separation enhances bimetallic catalysis of alcohol oxidation. *Nature* **2022**, *603*, 271-275.
10. Ryoo, R.; Kim, J.; Jo, C.; Han, S. W.; Kim, J.-C.; Park, H.; Han, J.; Shin, H. S.; Shin, J. W. Rare-earth–platinum alloy nanoparticles in mesoporous zeolite for catalysis. *Nature* **2020**, *585*, 221-224.
11. Liu, L.; Lopez-Haro, M.; Lopes, C. W.; Li, C.; Concepcion, P.; Simonelli, L.; Calvino, J. J.; Corma, A. Regioselective generation and reactivity control of subnanometric platinum clusters in zeolites for high-temperature catalysis. *Nat. Mater.* **2019**, *18*, 866-873.
12. Gorey, T. J.; Zandkarimi, B.; Li, G.; Baxter, E. T.; Alexandrova, A. N.; Anderson, S. L. Coking-Resistant Sub-Nano Dehydrogenation Catalysts: Pt_nSn_x/SiO_2 (n = 4, 7) *ACS Catal.* **2020**, *10*, 4543-4558.
13. Yang, F.; Wang, Y.; Cui, Y.; Yang, X.; Zhu, Y.; Weiss, C. M.; Li, M.; Chen, G.; Yan, Y.; Gu, M. D.; Shao, M. Sub-3 nm Pt@Ru toward Outstanding Hydrogen Oxidation Reaction Performance in Alkaline Media. *J. Am. Chem. Soc.* **2023**, *145*, 27500-27511.
14. Zhang, S.; Hao, Y.; Su, D.; Doan-Nguyen, V. V. T.; Wu, Y.; Sun, S.; Murray, C. B. Monodisperse Core/Shell Ni/FePt Nanoparticles and Their Conversion to Ni/Pt to Catalyze Oxygen Reduction. *J. Am. Chem. Soc*. **2014**, *136*, 15921-15924.
15. Alinezhad, A.; Gloag, L.; Benedetti, T. M.; Cheong, S.; Webster, R. F.; Roelsgaard, M.; Iversen, B. B.; Schuhmann, W.; Gooding, J. J.; Tilley, R. D. Direct Growth of Highly Strained Pt Islands on Branched Ni Nanoparticles for Improved Hydrogen Evolution Reaction Activity. *J. Am. Chem. Soc.* **2019**, *141*, 16202-16207.
16. Hirai, H.; Takano, S.; Nakashima, T.; Iwasa, T.; Taketsugu, T.; Tsukuda, T. Doping-Mediated Energy-Level Engineering of $M@Au_{12}$ Superatoms (M=Pd, Pt, Rh, Ir) for Efficient Photoluminescence and Photocatalysis. *Angew. Chem., Int. Ed.* **2022**, *61*, e202207290.

17. Dhital, R. N. Kamonsatikul, C.; Somsook, E. Bobuatong, K.; Ehara, M.; Karanjit, S.; Sakurai, H. Low-Temperature Carbon–Chlorine Bond Activation by Bimetallic Gold/Palladium Alloy Nanoclusters: An Application to Ullmann Coupling. *J. Am. Chem. Soc.* **2012**, *134*, 20250-20253.
18. Miura, H.; Tanaka, Y.; Nakahara, K.; Hachiya, Y.; Endo, K.; Shishido, T. Concerted Catalysis by Adjacent Palladium and Gold in Alloy Nanoparticles for the Versatile and Practical [2+2+2] Cycloaddition of Alkynes. *Angew. Chem., Int. Ed.* **2018**, *57,* 6136-6140.
19. Min, H.; Miyamura, H.; Yasukawa, T.; Kobayashi, S. Heterogeneous Rh and Rh/Ag bimetallic nanoparticle catalysts immobilized on chiral polymers. *Chem. Sci*. **2019**, *10*, 7619-7626.
20. Macht, J.; Janik, M. J.; Neurock, M.; Iglesia, E. Catalytic Consequences of Composition in Polyoxometalate Clusters with Keggin Structure. *Angew. Chem., Int. Ed.* **2007**, 46, 7864-7868.
21. Macht, J.; Janik, M. J. Neurock, M.; Iglesia, E. Mechanistic Consequences of Composition in Acid Catalysis by Polyoxometalate Keggin Clusters. *J. Am. Chem. Soc.* **2008**, *130*, 10369-10379.
22. Zuwei, X.; Ning, Z.; Yu, S.; Kunlan, L. Reaction-Controlled Phase-Transfer Catalysis for Propylene Epoxidation to Propylene Oxide. *Science* **2001**, *292*, 1139-1141.
23. Kamata, K.; Yonehara, K.; Sumida, Y.; Yamaguchi, K.; Hikichi, S.; Mizuno, N. Efficient Epoxidation of Olefins with ≥99% Selectivity and Use of Hydrogen Peroxide. *Science* **2003**, *300*, 964-966.
24. Nakagawa, Y.; Kamata, K.; Kotani, M.; Yamaguchi, K.; Mizuno, N. Polyoxovanadometalate-Catalyzed Selective Epoxidation of Alkenes with Hydrogen Peroxide. *Angew. Chem., Int. Ed.* **2005**, *44*, 5136-5141.
25. Song, G.; Wang, F.; Li, X. C–C, C–O and C–N Bond Formation via Rhodium(III)-Catalyzed Oxidative C–H Activation. *Chem. Soc. Rev.* **2012**, *41*, 3651–3678.
26. Arockiam, P. B.; Bruneau, C.; Dixneuf, P. H. Ruthenium(II)-Catalyzed C–H Bond Activation and Functionalization. *Chem. Rev.* **2012**, *112*, 5879–5918.
27. Gandeepan, P.; Müller, T.; Zell, D.; Cera, G.; Warratz, S.; Ackermann, L. 3d Transition Metals for C–H Activation. *Chem. Rev.* **2019**, *119*, 2192–2452.
28. Arshadi, S.; Banaei, A.; Monfared, A.; Ebrahimiasl, S.; Hosseinian, A. Cross-Dehydrogenative Coupling Reactions between Arenes (C–H) and Carboxylic Acids (O–H): A Straightforward and Environmentally Benign Access to O-Aryl Esters. *RSC Adv.* **2019**, *9*, 17101–17118.
29. Dalton, T.; Faber, T.; Glorius, F. C−H Activation: Toward Sustainability and Applications. *ACS Cent. Sci*. **2021**, *7*, 245–261.
30. Tian, T.; Li, Z.; Li, C.-J. Cross-Dehydrogenative Doupling: A Sustainable Reaction for C–C Bond Formations. *Green Chem.* **2021**, *23*, 6789–6862.
31. Docherty, J. H.; Lister, T. M.; Mcarthur, G.; Findlay, M. T.; Domingo-Legarda, P.; Kenyon, J.; Choudhary, S.; Larrosa, I. Transition-Metal-Catalyzed C–H Bond Activation for the Formation of C–C Bonds in Complex Molecules. *Chem. Rev.* **2023**, *123*, 7692–7760.
32. Gou, Q.; Tan, X.; Zhang, M.; Ran, M.; Yuan, T.; He, S.; Zhou, L.; Cao, T.; Luo, F. Cobalt-Catalyzed C–H Acetoxylation of Phenols with Removable Monodentate Directing Groups: Access to Pyrocatechol Derivatives. *Org. Lett.* **2020**, *22*, 1966–1971.
33. Okada, T.; Nobushige, K.; Satoh, T.; Miura, M. Ruthenium-Catalyzed Regioselective C–H Bond Acetoxylation on Carbazole and Indole Frameworks. *Org. Lett.* **2016**, *18*, 1150–1153.
34. More, N. Y.; Padala, K.; Jeganmohan, M. Ruthenium-Catalyzed C–H Benzoxylation of tert-Benzamides with Aromatic Acids by Weak Coordination. *J. Org. Chem.* **2017**, *82*, 12691–12700.
35. Liu, H.; Chi, W.; Dong, L. Ruthenium(II)-Catalyzed Sterically Hindered C–H Acyloxylation to Synthesize Biaryl Isoquinoline Derivatives via Peresters. *J. Org. Chem.* **2023**, *88*, 3148–3158.
36. Ye, Z.; Wang, W.; Luo, F.; Zhang, S.; Cheng, J. Rhodium-Catalyzed ortho-Benzoxylation of sp^2 C–H Bond. *Org. Lett*. **2009**, *11*, 3974–3977.
37. Wu, Y.; Zhou, B. Rhodium(III)-Catalyzed Selective C–H Acetoxylation and Hydroxylation Reactions. *Org. Lett.* **2017**, *19*, 3532–3535.
38. Mishra, A.; Vats, T. K.; Nair, M. P.; Das, A.; Deb, I. Rhodium-Catalyzed sp2 C–H Acetoxylation of N-Aryl Azaindoles/N-Heteroaryl Indolines. *J. Org. Chem.* **2017**, *82*, 12406–12415.
39. Zhai, W.; Li, B.; Wang, B. RhIII-Catalyzed Directed Selective C7-Hydroxylation and Acetoxylation of Indolines. *ChemistrySelect* **2018**, *3*, 8035–8039.
40. Jin, C.; Wang, G.; Yang, X.; Zhu, W.; Yang, Y. Experimental and Theoretical Studies on Rhodium-Catalyzed Direct C–H Benzoxylation Reaction. *Tetrahedron Lett.* **2018**, *59*, 2042–2045.
41. Wang, G.-W.; Yuan, T.-T.; Wu, X.-L. Direct Ortho-Acetoxylation of Anilides via Palladium-Catalyzed sp^2 C–H Bond Oxidative Activation. *J. Org. Chem*. **2008**, *73*, 4717–4720.
42. Gou, F.-R.; Wang, X.-C.; Huo, P.-F.; Bi, H.-P.; Guan, Z.-H.; Liang, Y.-M. Palladium-Catalyzed Aryl C–H Bonds Activation/Acetoxylation Utilizing a Bidentate System. *Org. Lett.* **2009**, *11*, 5726–5729.
43. Liu, Q.; Li, G.; Yi, H.; Wu, P.; Liu, J.; Lei, A. Pd-Catalyzed Direct and Selective C–H Functionalization: C3-Acetoxylation of Indoles. *Chem. Eur. J.* **2011**, *17*, 2353–2357.
44. Cook, A. K.; Sanford, M. S. Mechanism of the Palladium-Catalyzed Arene C–H Acetoxylation: A Comparison of Catalysts and Ligand Effects. *J. Am. Chem. Soc.* **2015**, *137*, 3109–3118.
45. Wu, J.; Hoang, K. L. M.; Leow, M. L.; Liu, X.-W. Pd-Catalyzed Cross-Coupling of Aromatic Compounds with Carboxylic Acids via C–H Bond Activation. *Org. Chem. Front.* **2015**, *2*, 502–505.
46. Li, W.-Q.; Yang, Q.-L.; Fang, P.; Mei, T.-S.; Zhang, D. Palladium-Catalyzed C(sp^2)–H Acetoxylation via Electrochemical Oxidation. *Org. Lett.* **2017**, *19*, 2905–2908.
47. Song, J.; Cui, J.; Liang, H.; Liu, Q.; Dong, Y.; Liu, H. Palladium-Catalyzed Direct Oxidative Esterification of Indoles at the C3 Position: A Novel Prospect for C(sp^2)–H Acyloxylation. *Asian J. Org. Chem.* **2018**, *7*, 341–345.
48. Mulligan, C. J.; Bagale, S. M.; Newton, O. J.; Parker, J. S.; Hii, K. K. M. Peracetic Acid: An Atom-Economical Reagent for Pd-Catalyzed Acetoxylation of C–H Bonds. *ACS Sustainable Chem. Eng.* **2019**, *7*, 1611–1615.
49. Flynn, K. M.; White, K. L.; Movassaghi, M. Directed Palladium-Catalyzed Acetoxylation of Indolines. Total Synthesis of N‑Benzoylcylindrocarine. *J. Org. Chem*. **2022**, *87*, 2975‑2984.
50. Qiu, D.; Zheng, Z.; Mo, F.; Xiao, Q.; Tian, Y.; Zhang, Y.; Wang, J. Gold(III)-Catalyzed Direct Acetoxylation of Arenes with Iodobenzene Diacetate. *Org. Lett.* **2011**, *13*, 4988–4991.
51. Pradal, A.; Toullec, P. Y.; Michelet, V. Gold-Catalyzed Oxidative Acyloxylation of Arenes. *Org. Lett.* **2011**, *13*, 6086–6089.
52. Matsumoto, K.; Tachikawa, S.; Hashimoto, N.; Nakano, R.; Yoshida, M.; Shindo, M. Aerobic C–H Oxidation of Arenes Using a Recyclable, Heterogeneous Rhodium Catalyst. *J. Org. Chem.* **2017**, *82*, 4305–4316.
53. Fiévet, F.; Ammar-Merah, S.; Brayner, R.; Chau, F.; Giraud, M.; Mammeri, F.; Peron, J.; Piquemal, J.-Y.; Sicard, L.; Viau, G. The polyol process: a unique method for easy access to metal nanoparticles with tailored sizes, shapes and compositions. *Chem. Soc. Rev.* **2018**, *47*, 5187–5233.
54. Ma, W.; Weng, Z.; Rogge, T.; Gu, L.; Lin, J.; Peng, A.; Luo, X.; Gou, X.; Ackermann, L. Ruthenium(II)-Catalyzed C–H Chalcogenation of Anilides. *Adv. Synth. Catal.* **2018**, *360*, 704–710.
55. Liang, Y.-F.; Yang, L.; Rogge, T.; Ackermann, L. Ruthenium(IV) Intermediates in C–H Activation/Annulation by Weak O-Coordination. *Chem. Eur. J.* **2018**, *24*, 16538–16552.
56. Naksomboon, K.; Poater, J.; Bickelhaupt, F. M.; Fernández-Ibáñez, M. Á. para-Selective C–H Olefination of Aniline

Derivatives via Pd/S,O-Ligand Catalysis. *J. Am. Chem. Soc.* **2019**, *141*, 6719–6725.

57. Rogge, T.; Oliveira, J. C. A.; Kuniyil, R.; Hu, L.; Ackermann, L. Reactivity-Controlling Factors in Carboxylate-Assisted C–H Activation under 4d and 3d Transition Metal Catalysis. *ACS Catal.* **2020**, *10*, 10551–10558.
58. Choi, I.; Messinis, A. M.; Ackermann, L. C7-Indole Amidations and Alkenylations by Ruthenium(II) Catalysis. *Angew. Chem., Int. Ed.* **2020**, *59*, 12534–12540.
59. Raziullah; Kumar, M.; Ahmad, A.; Dutta, H. S.; Rastogi, A.; Gangwar, M. K.; Koley, D. Ru-Catalyzed C–H Alkenylation on the Arene Ring of Pirfenidone Using Pyridone as a Directing Group. *Chem. Commun.* **2022**, *58*, 3481–3484.
60. Wang, L.; Carrow, B. P. Oligothiophene Synthesis by a General C–H Activation Mechanism: Electrophilic Concerted Metalation–Deprotonation (eCMD). *ACS Catal.* **2019**, *9*, 6821–6836.
61. Bjelopetrović, A.; Barišić, D.; Duvnjak, Z.; Džajić, I.; Kulcsár, M. J.; Halasz, I.; Martínez, M.; Budimir, A.; Babić, D.; Ćurić, M. A Detailed Kinetico-Mechanistic Investigation on the Palladium C−H Bond Activation in Azobenzenes and Their Monopalladated Derivatives. *Inorg. Chem.* **2020**, *59*, 17123–17133.
62. Evans, R.; Sampson, J.; Wang, L.; Lückemeier, L.; Carrow, B. P. Ligand Switchable Site Selectivity in C–H Alkenylation of Thiophenes by Turnover-Limiting Step Control. *Chem. Commun.* **2021**, *57*, 9076–9079.
63. Ren, P.; He, Z.; Xing, T.; Manar, K. K.; Sampson, J.; Jin, J.; Wang, L.; Carrow, B. P. Synthesis of π-Expanded Coumarins by Ligand-Enabled Selective C–H Functionalization. *Adv. Synth. Catal.* **2022**, *364*, 3155–3160.
64. Piszel, P. E.; Orzolek, B. J.; Olszewski, A. K.; Rotella, M. E.; Spiewak, A. M.; Kozlowski, M. C.; Weix, D. J. Protodemetalation of (Bipyridyl)Ni(II)–Aryl Complexes Shows Evidence for Five-, Six-, and Seven-Membered Cyclic Pathways. *J. Am. Chem. Soc.* **2023**, *145*, 8517–8528.
65. Tunge, J. A.; Foresee, L. N. Mechanistic Studies of Fujiwara Hydroarylation. C-H Activation versus Electrophilic Aromatic Substitution. *Organometallics* **2005**, *24*, 6440-6444.
66. Stokes, B. J.; Dong, H.; Leslie, B. E.; Pumphrey, A. L.; Driver, T. G. Intramolecular C-H Amination Reactions: Exploitation of the Rh_2(II)-Catalyzed Decomposition of Azidoacrylates. *J. Am. Chem. Soc.* **2007**, *129*, 7500-7501.
67. Mukhopadhyay, S.; Rothenberg, G.; Lando, G.; Agbaria, K.; Kazanci, M.; Sasson, Y. Air Oxidation of Benzene to Biphenyl – A Dual Catalytic Approach. *Adv. Synth. Catal.* **2001**, *343*, 455-459.
68. Garcia-Cuadrado, D.; de Mendoza, P.; Braga, A. A. C.; Maseras, F.; Echavarren, A. M. Proton-Abstraction Mechanism in the Palladium-Catalyzed Intramolecular Arylation: Substituent Effects. *J. Am. Chem. Soc.* **2007**, *129*, 6880-6886.
69. Pascual, S.; de Mendoza, P.; Braga, A. A. C.; Maseras, F.; Echavarren, A. M. Bidentate Phosphines as Ligands in the Palladium-Catalyzed Intramolecular Arylation: The Intermolecular Base-Assisted Proton Abstraction Mechanism. *Tetrahedron* **2008**, *64*, 6021-6029.
70. Frisch, M. J.; Trucks, G. W.; Schlegel, H. B.; Scuseria, G. E.; Robb, M. A.; Cheeseman, J. R.; Scalmani, G.; Barone, V.; Petersson, G. A.; Nakatsuji, H.; Li, X.; Caricato, M.; Marenich, A. V.; Bloino, J.; Janesko, B. G.; Gomperts, R.; Mennucci, B.; Hratchian, H. P.; Ortiz, J. V.; Izmaylov, A. F.; Sonnenberg, J. L.; Williams; ; Ding, F.; Lipparini, F.; Egidi, F.; Goings, J.; Peng, B.; Petrone, A.; Henderson, T.; Ranasinghe, D.; Zakrzewski, V. G.; Gao, J.; Rega, N.; Zheng, G.; Liang, W.; Hada, M.; Ehara, M.; Toyota, K.; Fukuda, R.; Hasegawa, J.; Ishida, M.; Nakajima, T.; Honda, Y.; Kitao, O.; Nakai, H.; Vreven, T.; Throssell, K.; Montgomery, J. A., Jr.; Peralta, J. E.; Ogliaro, F.; Bearpark, M. J.; Heyd, J. J.; Brothers, E. N.; Kudin, K. N.; Staroverov, V. N.; Keith, T. A.; Kobayashi, R.; Normand, J.; Raghavachari, K.; Rendell, A. P.; Burant, J. C.; Iyengar, S. S.; Tomasi, J.; Cossi, M.; Millam, J. M.; Klene, M.; Adamo, C.; Cammi, R.; Ochterski, J. W.; Martin, R. L.; Morokuma, K.; Farkas, O.; Foresman, J. B.; Fox, D. J. Gaussian 16 Rev. C.01; Gaussian, Inc.: Wallingford, CT, 2016.
71. Lee, C.; Yang, W.; Parr, R. G. Development of the Colle-Salvetti Correlation-Energy Formula into a Functional of the Electron Density. *Phys. Rev. B* **1988**, *37*, 785–789.
72. Becke, A. D. Density-Functional Thermochemistry. III., The Role of Exact Exchange. J. Chem. Phys. 1993, 98, 5648–5652.
73. Grimme, S.; Antony, J.; Ehrlich, S.; Krieg, H. A Consistent and Accurate Ab Initio Parameterization of Density Functional Dispersion Correction (DFT-D) for the 94 Elements H-Pu. *J. Chem. Phys*. **2010**, *132*, 154104.
74. Koyama, K.; Nagata, T.; Kudoh, S.; Miyajima, K.; Huitema, D. M. M.; Chernyy, V.; Bakker, J. M.; Mafuné, F. Geometrical Structures of Partially Oxidized Rhodium Cluster Cations, Rh6Om+ (m = 4, 5, 6), Revealed by Infrared Multiple Photon Dissociation Spectroscopy. *J. Phys. Chem. A* **2016**, *120*, 8599–8605.
75. Mafuné, F.; Koyama, K.; Nagata, T.; Kudoh, S.; Yasuike, T.; Miyajima, K.; Huitema, D. M. M.; Chernyy, V.; Bakker, J. M. Structures of Rhodium Oxide Cluster Cations $Rh_7O_m^+$ (m = 4-7, 12, 14) Revealed by Infrared Multiple Photon Dissociation Spectroscopy. *J. Phys. Chem. C* **2019**, *123*, 5964–5971.
76. Vásquez-Céspedes, S.; Wang, X.; Glorius, F. Plausible Rh(V) Intermediates in Catalytic C–H Activation Reactions. *ACS Catal.* **2018**, *8*, 242–257.
77. Li, Y.; Chen, H.; Qu, L.-B.; Houk, K. N.; Lan, Y. Origin of Regiochemical Control in Rh(III)/Rh(V)-Catalyzed Reactions of Unsaturated Oximes and Alkenes to Form Pyrdines. *ACS Catal.* **2019**, *9*, 7154–7165.
78. Jin, S.; Kim, J.; Kim, D.; Park, J.-W.; Chang, S. Electrolytic C–H Oxygenation via Oxidatively Induced Reductive Elimination in Rh Catalysis. *ACS Catal.* **2021**, *11*, 6590–6595.
79. Ishida, T.; Aikawa, S.; Mise, Y.; Akebi, R.; Hamasaki, A.; Honma, T.; Ohashi, H.; Tsuji, T.; Yamamoto, Y.; Miyasaka, M.; Yokoyama, T.; Tokunaga, M. Direct C–H Arene Homocoupling over Gold Nanoparticles Supported on Metal Oxides. *ChemSusChem* **2015**, *8*, 695–701.
80. Gao, L.; Feuillastre, S.; Clavier, G.; Pieters, G. Cross-Dehydrogenative Homocoupling of 2-Aryl-N-heterocycles and Application to the Synthesis of Phenylpyridine Borane Dimers. *Eur. J. Org. Chem.* **2022**, e202201164.

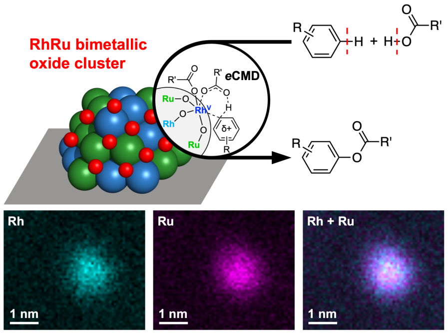
RhRu bimetallic oxide cluster
eCMD
R
H
+
H
O
R'
Ru
Rh
Rh^V
δ+
Rh
Ru
Rh + Ru
1 nm
1 nm
1 nm

TOC graphic